

- <sup>15</sup>M. C. Robinson and A. C. H. Hallett, *Can. J. Phys.* **44**, 2211 (1966).
- <sup>16</sup>J. Fontanella, C. Adeen, and D. Schuele, *Phys. Rev. B* **6**, 582 (1972).
- <sup>17</sup>R. S. Krishnan, *Progress in Crystal Physics* (Central Art Press, Chetput Madras, India, 1958), Vol. 1, p. 193.
- <sup>18</sup>A. J. Bosman and E. E. Havinga, *Phys. Rev.* **129**, 1593 (1963).
- <sup>19</sup>O. Rejler, S. Wernberg, and O. Beckman, *Arkiv Fysik* **32**, 509 (1966).
- <sup>20</sup>W. Känzig, H. R. Hart, and S. Roberts, *Phys. Rev. Letters* **13**, 543 (1964).
- <sup>21</sup>R. Fuchs, Technical Report No. 167, MIT Laboratory for Insulation Research, Massachusetts Institute of Technology, Cambridge, Mass., 1961 (unpublished).
- <sup>22</sup>B. Szigeti, *Proc. Roy. Soc. (London)* **A252**, 217 (1959).
- <sup>23</sup>E. E. Havinga and A. J. Bosman, *Phys. Rev.* **140**, A292 (1965).
- <sup>24</sup>G. Leibfried and W. Ludwig, in *Solid State Physics*, edited by F. Seitz and D. Turnbull (Academic, New York, 1961), Vol. 12, p. 367.
- <sup>25</sup>H. Fröhlich, *Theory of Dielectrics* (Oxford U.P., London, 1958), 2nd ed., p. 12.
- <sup>26</sup>E. E. Havinga, *J. Phys. Chem. Solids* **18**, 253 (1961).

## Impurity-Induced Raman Scattering in SrF<sub>2</sub> and BaF<sub>2</sub><sup>†</sup>

L. L. Chase,\* D. Kühner,<sup>‡</sup> and W. E. Bron

*Indiana University, Bloomington, Indiana 47401*

(Received 16 October 1972)

Measurements have been made of the impurity-induced Raman scattering spectra due to Eu<sup>2+</sup> impurities substituting for the cations in SrF<sub>2</sub> and BaF<sub>2</sub> single crystals. It is found that the data cannot be fitted to a nearest-neighbor coupling model as has been used previously to fit similar data in some alkali-halide hosts. An electron-phonon coupling model is presented in which purely Coulombic coupling is assumed so that the range of the coupling may be extended beyond the nearest neighbors without introducing new adjustable parameters. As a point-charge model is found insufficient to account for the relative intensities in the regions of acoustic- and optic-phonon scattering, extended charge distributions are assumed for the ionic shells. This treatment gives a qualitative fit to the gross intensity distribution of the observed spectra. However, the approximations used in the model result in some discrepancies between the calculated and observed spectra. It is concluded that the nearest-neighbor coupling model will give an adequate fit to the impurity-induced spectra only in hosts in which all ions in the unit cell vibrate with approximately equal amplitudes in the optic-phonon region.

### I. INTRODUCTION

The presence of isolated impurities in a crystal lattice breaks the lattice translational symmetry and therefore also breaks the  $\vec{k}$ -vector selection rule for Raman-scattering processes. Numerous experimental and theoretical investigations of such impurity-induced scattering processes<sup>1,2</sup> have been made both for systems in which the impurity strongly perturbs the vibrations of the host lattice, as well as for substitutional impurities which do not affect the host-lattice eigenfrequencies and eigenvectors. In the latter case, the impurity merely acts as a local optical-polarizability perturbation, and the impurity-induced phonon spectra are related to the density of vibrational states of the host lattice. However, the details of this relationship are a function of the character of the electronic states of the impurity complex and the perturbations of these states by lattice phonons. For example, the ground state and intermediate electronic states which determine the local polarizability of the complex may range from very localized states ( $4f^n$  levels of rare-earth ions, for ex-

ample) to energy bands of the host perturbed by the impurity. In the former case, the electron-phonon coupling may have a relatively short range, and a first-order treatment of the impurity-induced scattering in simple crystal lattices is a nearest-neighbor coupling model.<sup>1</sup> In this model the frequency dependence of the scattered intensity reproduces the projected density of phonon states on the nearest-neighbor ions. On the other hand, it is likely that a far more complex model will be required to treat the case of more extended impurity-electron states, and the scattered *intensity* will be less directly related to the phonon density of states, although the *positions* of sharp peaks in the density of states may still be obtained from such experiments.

A recent experimental<sup>1</sup> and theoretical<sup>1,2</sup> test of the nearest-neighbor coupling model for the Tl<sup>+</sup> impurity in several alkali-halide lattices led to generally good agreement between the model and the data, except for those crystals in which the cation and anion masses differ appreciably. For KBr: Tl<sup>+</sup> and KI: Tl<sup>+</sup>, for example, the observed intensity in the optical-mode region, although much

weaker in absolute intensity than that in the acoustic region, was nevertheless much more intense relative to the acoustic scattering than was predicted from the nearest-neighbor coupling model. These discrepancies would indicate that coupling to the second-nearest-neighbor K<sup>+</sup> ions, which have a larger vibrational amplitude in the optic-mode region than the heavier Br or I ions, cannot be ignored.

The fluorite lattices CaF<sub>2</sub>, SrF<sub>2</sub>, and BaF<sub>2</sub>, containing divalent rare-earth impurities provide an opportunity to further test the applicability of impurity-induced Raman scattering to probe the host-lattice phonon spectrum. The lattice dynamics of these crystals has been calculated from shell-model theories which have been tested recently by studies of phonon sidebands of the 4*f*<sup>*n*</sup> → 4*f*<sup>*n*</sup> electronic transitions of rare-earth impurities.<sup>3</sup> The Eu<sup>2+</sup> ion is a particularly good impurity for Raman-scattering experiments in SrF<sub>2</sub> and BaF<sub>2</sub>, because of its similarity in size and electronic configuration to the Sr<sup>2+</sup> and Ba<sup>2+</sup> ions. These properties are summarized in Table I, which lists the lattice constants and cation electronic configurations of CaF<sub>2</sub>, SrF<sub>2</sub>, BaF<sub>2</sub>, and EuF<sub>2</sub>. The Eu<sup>2+</sup> ion has strong electronic transitions from its 4*f*<sup>7</sup> (<sup>8</sup>S<sub>7/2</sub>) ground state to the many states of the 4*f*<sup>6</sup>5*d* configuration. These transitions begin above about 24 500 cm<sup>-1</sup> and extend into the ultraviolet region. They are thus displaced far enough from the 20 500 cm<sup>-1</sup> (4880 Å) argon-laser line for an off-resonance scattering treatment to be a good approximation. The transitions are electric dipole allowed and might accordingly be expected to be the major contribution to the local polarizability perturbation.

A major disadvantage to the fluorite lattices is the intense scattering from the Raman-allowed *T*<sub>2g</sub> vibration as well as some two-phonon scattering at higher frequencies. The latter may, however, be subtracted out by making use of data on pure samples. Both these scattering processes interfere with observations of the impurity-induced scattering. However, since the masses of the cations and anions in these hosts are so dissimilar, it is to be expected that the most significant departures from the predictions of the nearest-neighbor coupling model will be reflected in the relative intensities of the scattering in the acoustic and optic regions of the vibrational spectrum. Adequate data have been obtained to investigate this feature of the observed spectra, despite the obscuration of one prominent impurity scattering peak by the *T*<sub>2g</sub> mode scattering.

Since it is immediately apparent from the data displayed in Sec. II that the nearest-neighbor coupling model is insufficient to fit the observed spectra, a theory is presented in Sec. III in which

TABLE I. Cation electronic configurations and lattice constants of fluorite crystals.

Crystal	Configuration	Lattice constant (Å)
CaF <sub>2</sub>	[Ar]	5.44
SrF <sub>2</sub>	[Ar] 3 <i>d</i> <sup>10</sup> 4 <i>s</i> <sup>2</sup> 4 <i>p</i> <sup>6</sup>	5.78
BaF <sub>2</sub>	[Ar] 3 <i>d</i> <sup>10</sup> 4 <i>s</i> <sup>2</sup> 4 <i>p</i> <sup>6</sup> 4 <i>d</i> <sup>10</sup> 5 <i>s</i> <sup>2</sup> 5 <i>p</i> <sup>6</sup>	6.18
EuF <sub>2</sub>	[Ar] 3 <i>d</i> <sup>10</sup> 4 <i>s</i> <sup>2</sup> 4 <i>p</i> <sup>6</sup> 4 <i>d</i> <sup>10</sup> 4 <i>f</i> <sup>7</sup> 5 <i>s</i> <sup>2</sup> 5 <i>p</i> <sup>6</sup>	5.84

the coupling between the impurity electron and the host lattice phonons is due to a strictly Coulombic interaction. If a point-charge model is used, this assumption allows the inclusion of coupling to all the ions of the host without the introduction of additional parameters. The effects of polarization, which were not included in the work on alkali halides,<sup>1</sup> are also easily included in this treatment. It has also been found in the course of this work that a point-charge crystal-field coupling model is inadequate to fit the experimental results. By introducing an extended-charge distribution for the neighboring ions, which has a range reasonably consistent with the ionic radii, the resulting overlap between this charge distribution for the impurity electron leads to sizeable corrections which give a qualitative fit to the data. In Sec. IV, a comparison of the theoretical and experimental results is given, together with a discussion of the merits and possible difficulties of the theoretical approach.

## II. EXPERIMENT

Single-crystal samples of CaF<sub>2</sub>, SrF<sub>2</sub>, and BaF<sub>2</sub>, either pure or doped with up to 0.5 mole% of Eu<sup>2+</sup>, were obtained from Optovac Inc. The samples were x-ray oriented and mechanically polished so that four surfaces of the finished samples were (100) faces of the cubic fluorite structure, and the remaining surface was a (110) face. Appropriate polarization geometries were chosen so that the A<sub>1g</sub>, E<sub>g</sub>, and *T*<sub>2g</sub> phonon representations of the O<sub>h</sub> point group of these crystals could be examined. These geometries are summarized below,<sup>4</sup> where  $\vec{k}_i$  and  $\vec{k}_s$  are the incident- and scattered-light wave vectors,  $\hat{\epsilon}_i$  and  $\hat{\epsilon}_s$  are the incident- and scattered-light polarizations:

$$\begin{aligned}
 I(A_{1g}) + 4I(E_g) & \begin{cases} \vec{k}_i \parallel \langle 001 \rangle, \hat{\epsilon}_i \parallel \langle 100 \rangle \\ \vec{k}_s \parallel \langle 010 \rangle, \hat{\epsilon}_s \parallel \langle 100 \rangle \end{cases}, \\
 I(E_g) & \begin{cases} \vec{k}_i \parallel \langle 001 \rangle, \hat{\epsilon}_i \parallel \langle 110 \rangle \\ \vec{k}_s \parallel \langle 110 \rangle, \hat{\epsilon}_s \parallel \langle \bar{1}\bar{1}0 \rangle \end{cases}, \\
 I(T_{2g}) & \begin{cases} \vec{k}_i \parallel \langle 001 \rangle, \hat{\epsilon}_i \parallel \langle 100 \rangle \\ \vec{k}_s \parallel \langle 100 \rangle, \hat{\epsilon}_s \parallel \langle 010 \rangle \end{cases}.
 \end{aligned}$$

Most of the experiments were performed at 4.2 °K, although some data were obtained at 77 °K and were essentially identical to the 4.2 °K results. However, the usual corrections for thermal occupation of the phonon states were required at 77 °K for the low-frequency part of the impurity-induced scattering. All unused sample surfaces were coated black with a marker pen to avoid unwanted reflections of the incident laser light. Useable data were obtainable only with the 4880-Å line of the argon laser because intense fluorescence from trivalent rare-earth impurities, present in trace concentrations, was observed with most other major argon or krypton lines. However, with 4880-Å excitation and a power of 1 W only one or two sharp and weak fluorescence lines were observed in the region of two-phonon scattering in a few samples. These were easily identified because of their lack of polarization dependence. The scattered light was dispersed by a Spex model-1400 double monochromator and was detected with photon-counting techniques. A conventional multi-channel analyzer operating in the multiscaling mode was used to average several monochromator sweeps, and the data were punched on paper tape for computer processing.

The spectra are shown in Figs. 1 and 2 for BaF<sub>2</sub> and SrF<sub>2</sub>, respectively. At low frequencies we observe mainly impurity-induced scattering at  $T=4.2$  °K, while above the  $T_{2g}$  Raman mode both impurity-induced scattering and a more intense two-phonon scattering are observed. The large signal from the  $T_{2g}$  mode in the  $E_g$  and  $E_g + A_{1g}$  traces results from the large solid angle inherent in the  $f/1.5$  optical-detection system used to collect the scattered light. A reduced optical aper-

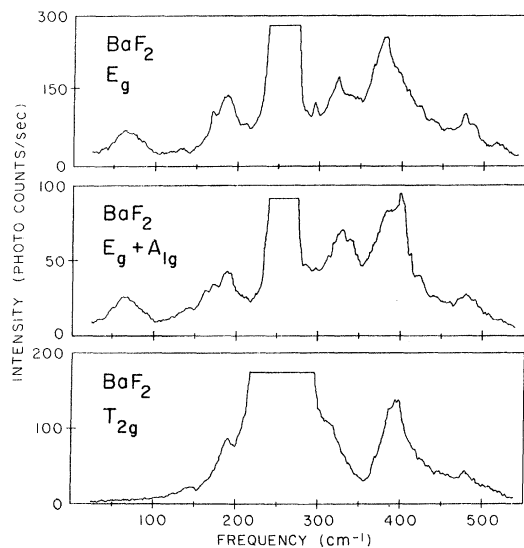


FIG. 1. Raman spectra of BaF<sub>2</sub>:Eu<sup>2+</sup>.

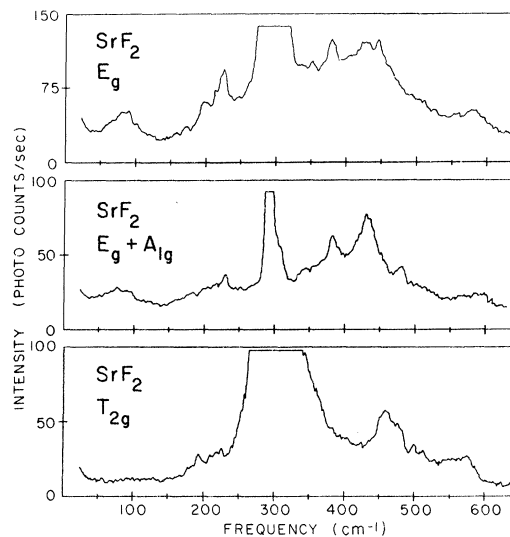


FIG. 2. Raman spectra of SrF<sub>2</sub>:Eu<sup>2+</sup>.

ture was used for several traces, but the consequent decrease in the  $T_{2g}$  intensity relative to the impurity-induced spectra was of little utility in this case, since a prominent impurity-induced peak, which is predicted to lie under the  $T_{2g}$  scattering, still could not be extracted easily from the data. There is, however, an observable peak on the high-frequency side of the  $T_{2g}$  mode which corresponds well in frequency, and roughly in relative intensity, with this predicted peak. We do not present the data obtained in CaF<sub>2</sub>, since the impurity-induced scattering was judged too weak to allow a meaningful comparison with the calculated spectra. Possible reasons for this relatively weak scattering in CaF<sub>2</sub> are discussed in Sec. IV.

The two-phonon scattering can be eliminated from Figs. 1 and 2 by subtracting from these traces the scattering observed in pure crystals using identical polarization geometries and other experimental conditions. Each datum point of the pure-crystal spectrum is multiplied by a single scaling constant, chosen to minimize the intensity of a prominent two-phonon peak. These corrections are easily facilitated once the data are recorded digitally on tape. This procedure is quite successful in removing nearly all traces of the two-phonon scattering, although it has very little beneficial effect on the  $T_{2g}$  mode, since its width increases somewhat in the doped samples. Because of this broadening, the corrected data points near the center of the  $T_{2g}$  mode become negative, and we have removed this feature in the corrected traces shown in Figs. 3 and 4. The correction process necessarily increases the noise level in the resulting traces, particularly in the optic-mode region above the  $T_{2g}$  peak. This is evident from the somewhat

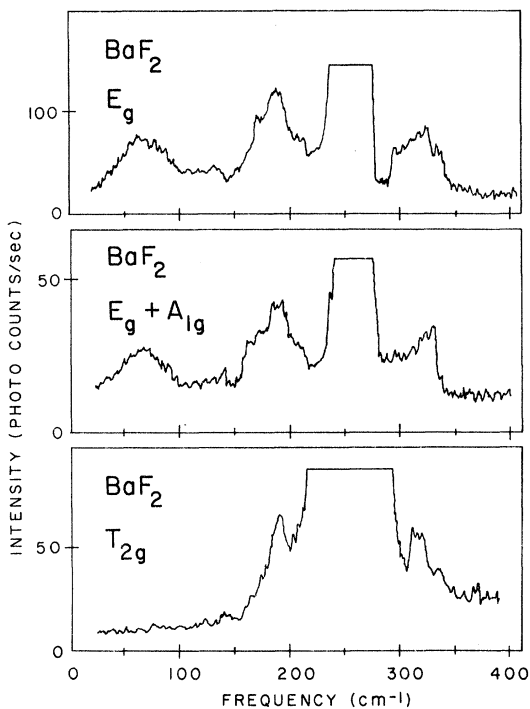


FIG. 3. Impurity-induced Raman spectra of  $\text{BaF}_2:\text{Eu}^{2+}$ . Suitably scaled spectra from a pure sample of  $\text{BaF}_2$  have been subtracted from these traces to eliminate the two-phonon spectra.

inconsistent shapes in  $E_g$  and  $E_g + A_{1g}$  scattering of the impurity-induced peak at  $300\text{--}350\text{ cm}^{-1}$  in  $\text{BaF}_2$ . Also, the peak at  $315\text{ cm}^{-1}$  in the  $T_{2g}$  spectrum of  $\text{BaF}_2$  coincides with a two-phonon peak of the pure crystal, and could not be completely suppressed by the subtraction process. For neither  $\text{BaF}_2$  nor  $\text{SrF}_2$  could evidence of the one expected prominent  $A_{1g}$  scattering peak be observed in the  $E_g + A_{1g}$  data. However, this peak would be at essentially the same position and would have nearly the same width as the peak in  $E_g$  scattering in the region of  $320\text{ cm}^{-1}$  for  $\text{BaF}_2$ . It can only be concluded that the  $A_{1g}$  symmetry scattering intensity is less than 50% of that for  $E_g$  symmetry.

The most interesting qualitative feature of the corrected data in Figs. 3 and 4 is the approximate equality of the intensities in the acoustic and optic regions. The delineation of these two regions on the traces is roughly at the position of the allowed  $T_{2g}$  Raman mode. Despite some uncertainty in the exact shape of the scattering in the optic-mode region due to the subtraction of the two-phonon peaks, the relative intensities displayed in Figs. 3 and 4 appear to be quite reproducible. Because of the large ratio of the masses of the Ba and Sr ions to that of the F ions, which are nearest neighbors to the  $\text{Eu}^{2+}$  impurities, the F ions would be expected to have a considerably larger vibrational amplitude

in the optic modes than in the acoustic modes. It is quite apparent, then, that the data show an enormous deviation from the expectations of the nearest-neighbor coupling model, and the primary challenge to any alternative to this model will be to account for this deviation.

## II. THEORY

### A. General Approach

We make use in these calculations of the perturbation-theoretic approach of Loudon.<sup>5</sup> However, for impurity-induced scattering, the initial, intermediate, and final electronic states involved in the virtual electronic transitions leading to the scattering process are localized states, as opposed to the band states considered by Loudon. This eliminates the  $\vec{k}$ -vector conservation requirement. The separation of the allowed and impurity-induced scattering is accomplished by assuming that the outer electronic shell ( $5s^2 5p^6$ ) of the  $\text{Eu}^{2+}$  ion is identical to that of the host cation ( $4s^2 4p^6$  for  $\text{Sr}^{2+}$  and  $5s^2 5p^6$  for  $\text{Ba}^{2+}$ ) so that there are no substantial changes in the valence- or conduction-band electronic structure. In that case, the perturbation-induced scattering is produced by the modulation of the polarizability of the inner  $4f^7$  configuration by the phonons.

The lattice force constants, which are determined mainly by the structure of the outer electronic shell, are assumed to remain unchanged at the  $\text{Eu}^{2+}$  site. Furthermore, the inversion symmetry at this site limits the perturbation-induced scattering to vibrational modes with even parity, for which the motion of the impurity is not involved in the electron-phonon coupling. Therefore no cor-

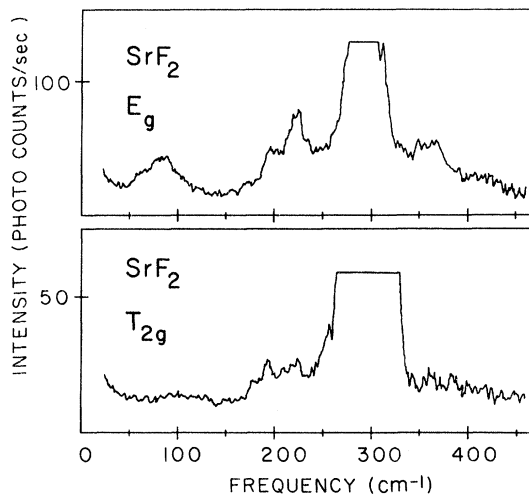


FIG. 4. Impurity-induced Raman spectra of  $\text{SrF}_2:\text{Eu}^{2+}$ . Suitably scaled spectra from a pure sample of  $\text{SrF}_2$  have been subtracted from these traces to eliminate the two-phonon spectra.

rections are required for the mass difference of the  $\text{Eu}^{2+}$  compared with  $\text{Sr}^{2+}$  or  $\text{Ba}^{2+}$ . These considerations allow the use of the eigenfrequencies and eigenvectors of the perfect lattice in the electron-phonon coupling problem. This procedure is justified both by the agreement of the data and calculations with regard to the positions of the peaks in the impurity-induced spectra and by previous studies of vibrational sidebands on the  $4f-4f$  electronic absorption spectra of  $\text{Sm}^{2+}$  and  $\text{Eu}^{2+}$  in the alkaline-earth halides.<sup>3</sup>

With these assumptions, the following expression is obtained for the intensity of the impurity-induced Raman scattering at  $T=0$ :

$$I(\omega_2)d\Omega = C \sum_{\vec{q}, \lambda} \left| \sum_{i, K} \sum_{j, k} R_k^{ij} \eta_k(l, K, \vec{q}, \lambda) e_1^i e_2^j \right|^2$$

$$R_k^{ij} = \sum_{\alpha, \beta} \left( \frac{p_{0\alpha}^i p_{\beta\alpha}^j [\gamma_{\alpha 0}^{iK}]_k}{[\omega_\beta + \omega(\vec{q}, \lambda) - \omega_1][\omega_2 + \omega(\vec{q}, \lambda)]} + \frac{p_{0\beta}^j p_{\beta\alpha}^i [\gamma_{\alpha 0}^{iK}]_k}{[\omega_\beta + \omega(\vec{q}, \lambda) + \omega_1][\omega_2 + \omega(\vec{q}, \lambda)]} \right. \\ \left. + \frac{p_{0\beta}^j [\gamma_{\beta\alpha}^{iK}]_k p_{\alpha 0}^i}{[\omega_\beta + \omega(\vec{q}, \lambda) - \omega_1](\omega_\alpha - \omega_1)} + \frac{p_{0\alpha}^i [\gamma_{\beta\alpha}^{iK}]_k p_{\alpha 0}^j}{[\omega_\beta + \omega(\vec{q}, \lambda) + \omega_2](\omega_\alpha + \omega_2)} \right. \\ \left. + \frac{[\gamma_{0\beta}^{iK}]_k p_{\beta\alpha}^j p_{\alpha 0}^i}{[\omega_\beta + \omega(\vec{q}, \lambda)](\omega_\alpha - \omega_1)} + \frac{[\gamma_{0\beta}^{iK}]_k p_{\beta\alpha}^i p_{\alpha 0}^j}{[\omega_\beta + \omega(\vec{q}, \lambda)](\omega_\alpha + \omega_2)} \right), \quad (2)$$

where  $p_{0\beta}^i$  is the matrix element of the  $i$  component of the impurity-electron momentum

$$p_{0\beta}^i = \langle 0 | p^i | \beta \rangle,$$

and  $\langle 0 |$  is the initial and  $\langle \alpha |$  is the intermediate electronic state of the impurity having energies  $\hbar\omega_\alpha$  and  $\hbar\omega_\beta$ , respectively.  $[\gamma_{\alpha\beta}^{iK}]_k$  is defined as the  $k$  component of

$$\vec{\gamma}_{\alpha\beta}^{iK} = \langle \alpha | \vec{u}_{iK}^{(1)} | \beta \rangle,$$

where  $\vec{u}_{\alpha\beta}^{(1)}$  is the electron-phonon coupling field, which is the first-order term of the electron-phonon coupling potential expansion with respect to the displacement of the ion at  $\vec{R}_{iK}^0$  from its equilibrium position.

The energies of the  $4f^6 5d$  states extend from about 24 500 to about 40 000  $\text{cm}^{-1}$ ,<sup>6</sup> whereas the frequency of the incident light is 20 500  $\text{cm}^{-1}$ . It follows that the second, fourth, and sixth terms in Eq. (2) are small in comparison with the others. The third term is the largest of those remaining, although the first and fifth are not negligible. Because little is known of the detailed nature of the set of states  $\langle \alpha |$  and  $\langle \beta |$  and, therefore, of  $\vec{\gamma}_{\alpha\beta}^{iK}$  as a function of  $\omega_\alpha$  and  $\omega_\beta$ , the dependence of  $R_k^{ij}$  on  $\omega(\vec{q}, \lambda)$  must be neglected. It is apparent from the

$$\times \delta(\omega_1 - \omega(\vec{q}, \lambda) - \omega_2) d\Omega, \quad (1)$$

where  $C$  is a coefficient involving the incident and scattered frequencies, the incident intensity, the impurity concentration, and other constants; the first sum is over the  $\lambda$  phonon branch with wave vector  $\vec{q}$ ; the second sum is over all ions  $K$  ( $K=1$  for the cation,  $K=2, 3$  for the anions) in the unit cell  $l$ , except the impurity ion itself.  $R_k^{ij}$  is the Raman tensor for a single impurity;  $\eta_k(l, K, \vec{q}, \lambda)$  is the  $k$  component of the eigenvector of ion  $l, K$ ;  $e_1^i$  and  $e_2^j$  denote the  $i$  and  $j$  polarization components of the incident and scattered light waves with frequencies  $\omega_1$  and  $\omega_2$ , respectively;  $d\Omega$  is the solid angle. The Raman tensor is given by

energy denominator of the third term in Eq. (2) that this approximation will lead to a slight decrease in the calculated intensity in the region of low phonon frequencies relative to the intensity at higher frequencies. Although such a deviation is observed between the calculated and measured spectra, it is much larger than the highest possible decrease of a few percent owing to the neglect of  $\omega(\vec{q}, \lambda)$ .

## B. Electron-Phonon Coupling Field

It is shown in this section that symmetry considerations, and the approximation that the  $4f^7$  and  $4f^6 5d$  electrons are well localized at the  $\text{Eu}^{2+}$  site compared with the nearest-neighbor distance, allows the factorization of the matrix elements  $\vec{\gamma}_{\alpha\beta}^{iK}$  of the electron-phonon coupling field so that the calculation of the field can be separated from the integration over the impurity-electron coordinates.

The electron-phonon coupling potential  $u(\vec{r}, \vec{R}_{iK})$ , where  $\vec{r}$  is the electron coordinate measured relative to the  $\text{Eu}^{2+}$  core, can be expanded in the displacements  $\Delta\vec{R}_{iK}$  of the ions from their equilibrium positions  $\vec{R}_{iK}^0$ :

$$u(\vec{r}, \vec{R}_{iK}) = u^{(0)}(\vec{r}, \vec{R}_{iK}^0) + \sum_{i, K} \vec{u}_{iK}^{(1)} \cdot \Delta\vec{R}_{iK} + O(\Delta R_{iK}^2), \quad (3)$$

in which it is understood that  $\vec{u}_{iK}^{(1)}$  is a function of  $\vec{r}$  and the equilibrium position  $\vec{R}_{iK}^0$ . The second- and higher-order terms in  $\vec{\Delta}\vec{R}_{iK}$  are neglected in the one-phonon scattering process.  $u(\vec{r}, \vec{R}_{iK})$  transforms as the unit representation of the  $O_h$  point group symmetry at the Eu<sup>2+</sup> site. Therefore  $\vec{u}_{iK}^{(1)}$  transforms according to the same representation as  $\vec{\Delta}\vec{R}$ . The symmetry operators transform the electronic space as well as the lattice space. For the use of matrix-element selection rules, only the transformation properties of  $\vec{u}_{iK}^{(1)}$  with regard to the electronic coordinate are important.  $u_{iK}^{(1)}$  may be expanded in a power series in the  $\vec{R}_{iK}^0$  in which  $\vec{R}_{iK}^0$  and each power of  $\vec{R}_{iK}^0$  transforms according to the unit representation. Hence  $\vec{u}_{iK}^{(1)}$  transforms in the electronic space, as does  $\vec{\Delta}\vec{R}_{iK}$  in the lattice space.

The standard method of introducing symmetry features into the electric-phonon coupling field is by the decomposition of  $\vec{\Delta}\vec{R}_{iK}$  into irreducible representations. The above considerations reveal that the same goal is achieved by decomposing  $\vec{u}_{iK}^{(1)}$  into irreducible representations with regard to electronic space. A simple way to do this is to first expand  $\vec{u}_{iK}^{(1)}$  into spherical harmonics as

$$\vec{u}_{iK}^{(1)} = \sum_{nm} \vec{a}_{nm}^{iK} Y_{nm}(\theta, \varphi), \quad (4)$$

where

$$\vec{a}_{nm}^{iK}(\vec{r}, \vec{R}_{iK}^0) = \int \vec{u}_{iK}^{(1)}(\vec{r}, \vec{R}_{iK}^0) Y_{nm}^*(\theta, \varphi) d\Omega, \quad (5)$$

$\theta$  and  $\varphi$  are the angular coordinates of the electron, and  $r = |\vec{r}|$ .

The spherical harmonics are then used to construct the  $\gamma$  component of the  $s$  irreducible representation,  $\Gamma$ , of the point group of the impurity:

$$\Phi_n^{s\Gamma\gamma}(\theta, \varphi) = \sum_m \sigma_{nm}^{s\Gamma\gamma} Y_{nm}(\theta, \varphi), \quad (6)$$

where  $\sigma_{nm}^{s\Gamma\gamma}$  are easily deduced, or are given by Ballhausen.<sup>7</sup>

The  $\vec{a}_{nm}^{iK}$  may be expanded about  $r=0$  as

$$\vec{a}_{nm}^{iK} = \vec{c}_{nm}^{(0)IK} + \vec{c}_{nm}^{(1)IK} r + \vec{c}_{nm}^{(2)IK} r^2 + O(r^3), \quad (7)$$

and the introduction of the point-group symmetry representation leads to

$$\vec{c}_{ns\Gamma\gamma}^{(p)IK} = \sum_m \sigma_{nm}^{s\Gamma\gamma} \vec{c}_{nm}^{(p)IK}. \quad (8)$$

If the electronic wave functions are well localized at the Eu<sup>2+</sup> compared with the nearest-neighbor distance  $R_0$ , only the lowest-order terms in  $r$  are important for the calculation of the matrix elements  $\gamma\alpha\beta$ . For example, if  $u(\vec{r}, \vec{R}_{iK})$  is a Coulomb potential, the successive terms decrease by a factor of  $r/R_0$ . When the expansion is terminated beyond the quadratic terms in  $r$ , all  $\vec{a}_{nm}^{iK}(r, R_0)$  are zero for  $n > 2$  and the electron-phonon coupling field is composed of monopolar, dipolar, and quadrupolar fields.

The monopolar field transforms as  $A_{1g}$  and contains a constant term and one quadratic in  $r$ . The constant term shifts the energies of all levels equally and can be neglected. In a point-charge crystal-field model for the electron-phonon coupling, only this constant coefficient would be nonzero for the monopole field. However, this is not true for the extended-charge model discussed below. The quadrupolar field is quadratic in  $r$  and, since  $Y_{2m}(\theta, \varphi)$  can be decomposed into one  $E_g$  and one  $T_{2g}$  representation, the  $E_g$  and  $T_{2g}$  symmetry phonon spectra result from this term. Since each representation occurs only once in this order of approximation, the index  $s$  is omitted from the following discussion.

Combining Eqs. (2), (4), (5), (6), (7), (8), the separation of the scattering with respect to the point-group symmetry is given by

$$I_\Gamma(\omega_2) = c \left| \sum_{i,j,\gamma} R_{i\gamma}^{ij} e_1^i e_2^j \right|^2, \quad (9)$$

where

$$R_{i\gamma}^{ij} = \sum_{\alpha,\beta,n} \left( \frac{p_{0\beta}^i p_{\beta\alpha}^j \langle \alpha | r^2 \Phi_n^{\Gamma\gamma}(\theta, \varphi) | \beta \rangle}{(\omega_\beta - \omega_1)\omega_2} + 5 \text{ other terms} \right) \sum_{\vec{q}\lambda} \left( \frac{1}{\omega(\vec{q}, \lambda)} \right)^{1/2} \left( \sum_K \vec{K}_{i\gamma}^{0K} \cdot \vec{\epsilon}_K(\vec{q}, \lambda) \right) \delta(\omega - \omega(\vec{q}, \lambda) + \omega_2), \quad (10)$$

where

$$\vec{K}_{i\gamma}^{0K} = \sum_l \vec{c}_{n\Gamma\gamma}^{(2)IK} e^{i\vec{q} \cdot \vec{R}_{iK}^0} \quad (11)$$

$\vec{\epsilon}_K(\vec{q}, \lambda)$  is the mass-reduced polarization vector for ion  $K$ , which is related to the eigenvector by the well-known relation

$$\vec{\eta}_{iK}(\vec{q}, \lambda) = \vec{\epsilon}_K(\vec{q}, \lambda) e^{i\vec{q} \cdot \vec{R}_{iK}^0}. \quad (12)$$

In Eq. (10) the calculation of the matrix elements is now totally separated from the electron-phonon

coupling field which is given by  $\vec{c}_{n\Gamma\gamma}^{(2)IK}$  if only the monopolar and quadrupolar fields are involved. The relative intensities  $I(A_{1g})$ ,  $I(E_g)$ , and  $I(T_{2g})$  cannot be obtained without calculating these matrix elements. However, for the dependence of each of these intensities on the phonon frequency, the first sum in Eq. (10) is simply a multiplying factor for each representation, and the frequency distribution of each  $I^\Gamma(\omega)$  can be calculated, in principle, with no adjustable parameters if the electron-phonon coupling model allows the calculation of  $\vec{c}_{n\Gamma\gamma}^{(2)IK}$  from

$$\begin{aligned}
& + c_{F\gamma}^{IK}(\lambda_K) e^{i\vec{q}\cdot\vec{R}_{IK}^0} Z_{KS}] \cdot \vec{\epsilon}_K(q, \lambda) \\
& + \vec{c}_{F\gamma}^{IK}(\lambda_K) \cdot e^{i\vec{q}\cdot\vec{R}_{IK}^0} \vec{P}_K(\vec{q}, \lambda) \} . \quad (16)
\end{aligned}$$

The first term of the summation in Eq. (16) is the coupling to the rigid ion, and the second term is the coupling to the polarization. If the shells are assumed to contain eight electrons, two parameters  $\lambda_1$  and  $\lambda_2$ , are required to describe the total electron-phonon interaction.

#### IV. DISCUSSION

##### A. Comparison of Calculated and Observed Spectra

The lattice vibration eigenfrequencies and eigenvectors were calculated from a modified shell model<sup>3</sup> with parameters derived from elastic constant data, dielectric constant data, and the allowed Raman frequencies,<sup>8</sup> all obtained at 77° K or below. A general picture of the results obtained for the calculated impurity-induced Raman scattering intensity is given in Fig. 5. Figure 5(a) shows the  $E_g$  spectra of BaF<sub>2</sub> calculated from a point-charge model for the electron-phonon coupling ( $\lambda_1 = \lambda_2 = \infty$ ), and in Fig. 5(b) is the calculation for an extended charge model where  $r_K = \lambda_K^{-1}$ . The values of  $r_K$  are in units of the F-F spacing along a cube axis, which is one-half the lattice constant. The dotted lines in the figure are calculated with equal core and shell displacements, that is  $\vec{P}_K(\vec{q}, \lambda) = 0$  in Eq. (16). This neglect of the ionic polarization in the electron-lat-

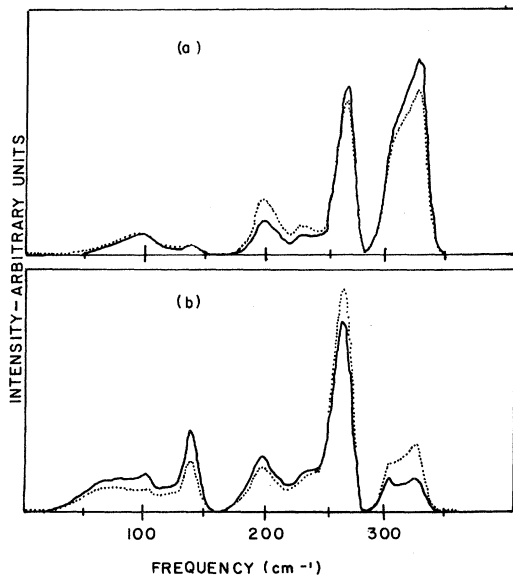


FIG. 5. Comparison of the calculated  $E_g$  symmetry impurity-induced scattering intensity of BaF<sub>2</sub>:Eu<sup>2+</sup> for (a) a point-charge model and (b) an extended-charge model with  $r_1 = 0.20$  and  $r_2 = 0.15$  (for explanation, see text).

tice coupling is an approximation used by Harley *et al.*<sup>1</sup> in the nearest-neighbor rigid-ion coupling model. The solid lines include the effects of the polarization in the electron-lattice coupling. From these curves it is clear that the extended-charge model leads to both a large change in the relative intensities in the acoustic and optic regions as well as a reversal of the contribution of ionic polarization to the intensities in these regions. The former effect can be explained by the larger overlap of the nearest-neighbor F ions at the Eu<sup>2+</sup> core compared with the next-nearest Ba<sup>2+</sup> ions. This reduces the coupling to the large F vibrational amplitude in the optic modes, whereas the acoustic coupling is not so strongly affected since the Ba<sup>2+</sup> and F vibrate with roughly equal amplitudes in the acoustic modes. The large effect of this overlap is due to the fact that the full shell charge of  $-8|e|$  is distributed as in Eq. (14), whereas the formal F charge is  $-|e|$  in the point-charge calculation in Fig. 5(a). The effects of the distribution can be understood by considering the effective charge contained in a spherical region centered about a neighboring ion and having a radius equal to the distance of that ion from the Eu<sup>2+</sup> impurity. For large enough  $r_K$ , this effective shell charge of the nearest-neighbor F ions is reduced such that the positive core charge dominates the coupling. A simple argument shows that this reversal of the sign of the effective charge of an ion will also lead to a reversal of the contribution of the polarization of that ion to the scattered intensity as is obtained in Fig. 5(b). The reversal of the sign of the effective charge of the nearest neighbors also leads to values of  $r_2$  for the F ions such that the calculated intensities of the optic-mode peaks, at 325 cm<sup>-1</sup> in BaF<sub>2</sub> or 350 cm<sup>-1</sup> in SrF<sub>2</sub>, pass through zero. It is, therefore, possible to fit the relative intensities of the acoustic- and optic-mode peaks with *two* values of  $\lambda_2$  slightly less than or slightly greater than the values of  $r_2$  which produce a zero intensity in the optic-mode peaks. We find that the larger of these two values of  $r_2$  gives a slightly better over-all fit to the spectra for both SrF<sub>2</sub> and BaF<sub>2</sub>.

The calculations are compared with the measured spectra for BaF<sub>2</sub> and SrF<sub>2</sub> in Figs. 6–9. Since the intensity scales in the calculated spectra are arbitrary, only relative intensities of the various features are significant, and the solid curves, which include the effects of polarization, are to be compared with the data. The values of  $r_1 = 0.20$  and  $r_2 = 0.15$  used in the calculations give the best fit to the relative intensities in the acoustic and optic regions and correspond, respectively, to approximately one-half of the ionic radii of the cations and the fluorine ion.

It is clear that the point-charge model for the  $E_g$  spectra in Fig. 5(a) would give a very poor fit to the

first principles. The assumption of a point-charge Coulombic coupling discussed below enables this to be done even when the shell and core eigenvectors of all the ions in the crystal are coupled to the impurity. If such a simple interaction is not chosen, a separate coupling parameter would be required in Eq. (1) for every representation of each set of ions at equivalent  $\vec{R}_{lK}$ . The disadvantage of the latter approach is that the extension of the coupling beyond the nearest neighbors leads to a great number of unknown parameters and to an elaborate calculation of symmetry vectors and their projection onto the eigenvectors. For example, the 12 next-nearest-neighbor  $M^{2+}$  ions in  $MF_2$  have two representations each of  $E_g$  and  $T_{2g}$  symmetry and one of  $A_{1g}$  symmetry. Thus, as many as nine parameters would be required to treat just the nearest- and next-nearest-neighbor core coordinates, and a separate coupling to the shells would double this. The disadvantages to the approach used here are summarized in Sec. IV.

### C. Coupling Model

The ideal lattice dynamics of the alkaline-earth halides is calculated on the basis of a modified

$$u_{nm}(\vec{r}, \vec{R}_{lK}) = \sum_{iK} \frac{4\pi e^2}{2n+1} \left( r^{-(n+1)} \int_0^r r'^i \rho(\vec{r}' - \vec{R}_{lK}) Y_{nm}^*(\theta', \varphi') d^3 \vec{r}' + r^n \int_r^\infty (r')^{-(n+1)} \rho(\vec{r}' - \vec{R}_{lK}) Y_{nm}^*(\theta', \varphi') d^3 \vec{r}' \right), \quad (13)$$

where  $\rho(\vec{r}' - \vec{R}_{lK})$  is the charge distribution of the ion  $l, K$ . If it is assumed that the charge distributions of the neighboring ions do not overlap the impurity electron, only the second term of Eq. (13) is nonzero, giving the usual point-charge crystal-field expansion about the impurity site. In the course of this work, it was found that this approximation was insufficient to fit the observed spectra, and a charge distribution of the form

$$\rho(\vec{r}' - \vec{R}_{lK}) = (Z_{KS} \lambda_K^3 / 8\pi) e^{-\lambda_K |\vec{r}' - \vec{R}_{lK}|} \quad (14)$$

was chosen for the shell charge distribution of ion  $l, K$ .  $Z_{KS} = -8|e|$  is the total shell charge. The cores are assumed to be point charges with  $Z_{1C} = +10|e|$  for the  $M^{2+}$ , and  $Z_{2C} = Z_{3C} = +7|e|$  for the two F ions. Although this charge distribution has a long-range behavior similar to that of a Slater function, we offer no justification for it other than the fact that it is a physically reasonable and a mathematically simple means of allowing for the spatial extent of the neighboring ions. Although another two parameters giving the range of the charge distributions,  $\lambda_1$  and  $\lambda_2 = \lambda_3$ , are introduced into the theory, and calculated spectra are relatively insensitive to  $\lambda_1$  (for the second-nearest-neighbor cations), and both  $\lambda_1$  and  $\lambda_2$  should be comparable to the ionic radii of the  $M^{2+}$  and F<sup>-</sup> ions, respective-

ly. The modification involves a change in the effective ionic polarizability as discussed in Ref. 3 (see Sec. VA 1). The classical shell models assume a point-charge core and a rigid shell which are coupled to each other by means of a harmonic spring. The core-shell interaction between different ions is assumed to be purely Coulombic. The shell-shell interaction includes both a classical Coulomb interaction and a parametrized interaction due to overlapping effects; nevertheless, the shells themselves are assumed to be nonoverlapping. Basically, the same assumptions are made in the quantum-mechanically derived shell models; yet, the overlapping effects are described by pseudopotentials. Altogether, the pseudopotential contains the interaction obtained from classical Coulombic overlap, exchange and effects due to orthogonalization. These interactions are important for the outer electrons of the  $Eu^{2+}$  impurity. However, for the inner electrons, exchange and orthogonalization effects may be negligible, and only the classical Coulombic interaction will be considered in this discussion.

The coefficient of  $Y_{nm}(\theta, \varphi)$  in the spherical harmonic expansion of the Coulomb potential about the  $Eu^{2+}$  site is the well-known expression

ly.

The symmetrized coupling coefficients for this charge distribution are found to be

$$\begin{aligned} \vec{c}_n^{(2)lK}(A_{1g}) &= \frac{1}{12} (4\pi)^{1/2} e^2 \lambda_K^3 \vec{\nabla}_{lK} [Y_{00}(\vec{R}_{lK}) e^{-\lambda_K R_{lK}}], \\ \vec{c}_n^{(2)lK}(\Gamma, \gamma) &= \frac{1}{5} (4\pi)^{1/2} e^2 \vec{\nabla}_{lK} \left\{ [\Phi_n^{\Gamma\gamma}(\vec{R}_{lK})]^* \right. \\ &\quad \left. \times R_{lK}^{-3} \left[ 1 - e^{-\lambda_K R_{lK}} \sum_{v=0}^3 \frac{(\lambda_K R_{lK})^v}{v!} \right] \right\}, \end{aligned} \quad (15)$$

where  $\Gamma$  in the second expression is either  $E_g$  or  $T_{2g}$ ,  $\vec{\nabla}_{lK}$  is a gradient with respect to  $\vec{R}_{lK}$ ,  $R_{lK} = |\vec{R}_{lK}|$ , and  $\Phi_n^{\Gamma\gamma}(\vec{R}_{lK})$  are given by Eq. (6). The coupling coefficients for the ion cores are obtained in the limit  $\lambda_K \rightarrow \infty$ . These relations are for a unit shell or core charge.

It is important to note that, according to the shell model, the polarization of the ions results from the shift of the shell relative to the core. The core displacement is given by  $\vec{\epsilon}_K(\vec{q}, \lambda)$  and the polarization by  $\vec{P}_K(q, \lambda)$ , which is uniquely determined by  $\vec{\epsilon}_K(\vec{q}, \lambda)$ . Therefore the following relation is evident:

$$\vec{R}_{lK}^{lK} \cdot \vec{\epsilon}_K(\vec{q}, \lambda) = \sum_l \{ [\vec{c}_{lK}^{lK}(\lambda_K = \infty) e^{i\vec{q} \cdot \vec{R}_{lK}^0} Z_{lK} \}$$

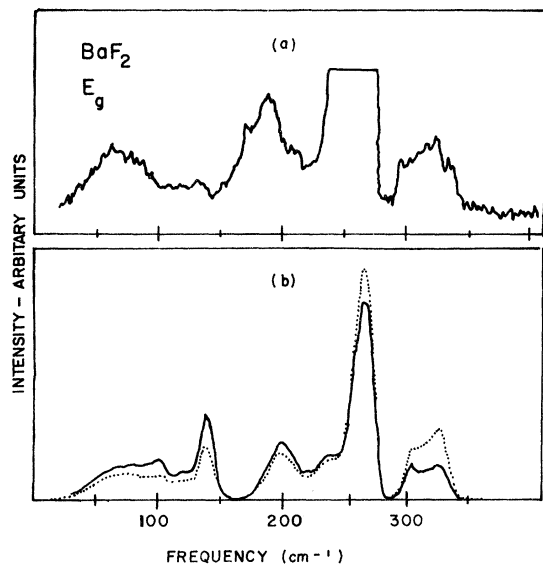


FIG. 6. Comparison of (a) the  $E_g$  scattering data for BaF<sub>2</sub>:Eu<sup>2+</sup> and (b) the calculated scattering with  $r_1 = 0.20$  and  $r_2 = 0.15$ .

data, because of the relatively large intensity in the peaks observed in the vicinity of 325 cm<sup>-1</sup> in BaF<sub>2</sub> and 350 cm<sup>-1</sup> in SrF<sub>2</sub>. Also, the position of the lowest-frequency peak in the acoustic region is at about 90 cm<sup>-1</sup> for the point-charge model, compared with its position at 65 cm<sup>-1</sup> in the BaF<sub>2</sub> data. Although the calculation including extended shell charges corrects these difficulties, it gives a poor fit to the shape of the spectrum in the acoustic re-

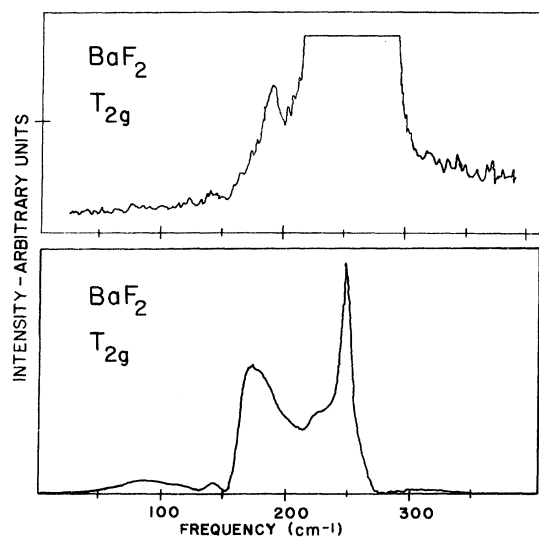


FIG. 7. Comparison of the  $T_{2g}$  scattering data for BaF<sub>2</sub>:Eu<sup>2+</sup> (upper curve) and the calculated scattering with  $r_1 = 0.20$  and  $r_2 = 0.15$  (lower curve).

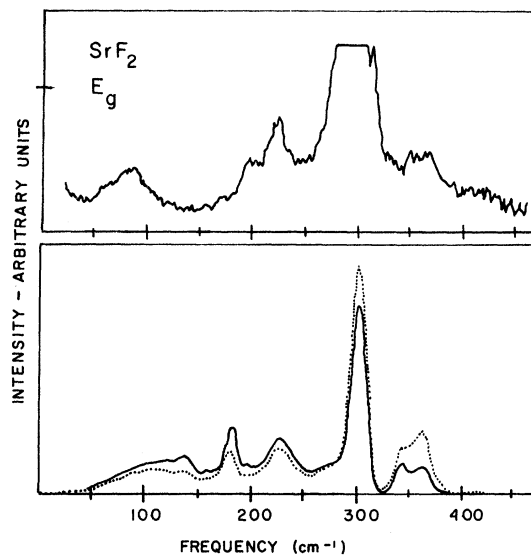


FIG. 8. Comparison of the  $E_g$  scattering data for SrF<sub>2</sub>:Eu<sup>2+</sup> (upper curve) and the calculated scattering with  $r_1 = 0.20$  and  $r_2 = 0.15$  (lower curve).

gion. In particular, the peak rising to a gradual maximum at about 70 cm<sup>-1</sup> in BaF<sub>2</sub> continues to much higher frequency in the calculated spectrum than in the data. Of greater concern is the amplification by the extended charge model of a peak at about 135 cm<sup>-1</sup> in BaF<sub>2</sub>, which is relatively weak in both the data and in the point-charge calculation. This peak clearly dominates in intensity in the region below 250 cm<sup>-1</sup> in the extended charge calculation of Fig. 6 for both the dotted and solid curves.

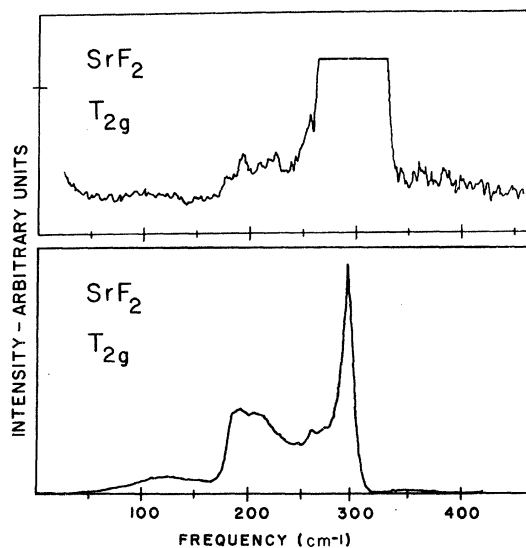


FIG. 9. Comparison of the  $T_{2g}$  scattering data for SrF<sub>2</sub>:Eu<sup>2+</sup> (upper curve) and the calculated scattering with  $r_1 = 0.20$  and  $r_2 = 0.15$  (lower curve).

It is not possible to fit the relative intensities of the other peaks in the data by varying  $r_1$  and  $r_2$  without producing this effect.

The  $T_{2g}$  scattering data and calculations in Figs. 7 and 9 provide little opportunity for further comparison of the two models, since only one impurity-induced peak is observed below the allowed Raman mode.

### B. Effects of Approximations

The three principal assumptions made in the electron-phonon coupling model are (1) the coupling is Coulombic with classical charge overlap; (2) the electronic states (initial and intermediate) which cause the change in local polarizability are well localized near the impurity nucleus compared with the nearest-neighbor distance, so that the coupling can be calculated from the gradient of the potential at the origin,  $r=0$ ; and (3) only the monopolar and quadrupolar terms in the potential expansion are considered, because the higher-order terms fall off rapidly for  $r \ll |\vec{R}_{iK}|$  in Eq. (5).

In fact, none of these assumptions can be firmly justified for the system under consideration here. The use of a classical charge overlap by Kleiner<sup>9</sup> led to a crystal-field splitting of the wrong sign for chromium alum, and this difficulty can only be corrected by a molecular-orbital approach,<sup>10</sup> which allows for exchange and orthogonalization of the impurity electron with the ligand shell electrons. Furthermore, the intermediate states involve the  $5d$  configuration, which is in the outer shell of the Eu<sup>2+</sup> ion. These considerations would also appear to invalidate approximation (3), at least for the part of the coupling due to the nearest-neighbor shells, which would have a large overlap with the  $5d$  states.

However, a simple calculation of the effects of the charge overlap suggests that the parameter  $r_2$  essentially leads to an effective coupling coefficient for the nearest-neighbor F ion shells, while the coupling to all other ions and shells remains nearly the same as in the point-charge calculation. For instance, for  $r_2=0.15$ , the effective shell charge of the nearest F ions is  $-7.3$ , whereas that of the second-nearest F ions along  $[112]$  directions is essentially the full  $-8$ . With  $r_1=0.20$  the nearest Ba<sup>2+</sup> effective shell charge is reduced to  $-7.75$ . Thus the solid curves for the rigid-ion coupling in Fig. 5(b) are calculated for effective ionic charges  $Z_{iS}^{eff} + Z_{iC}$  of  $+0.3$ ,  $-1.0$ , and  $+2.25$  for the nearest F, next-nearest F, and nearest Ba ions, respectively. It is clear that the overlap effects mainly adjust the effective charges of the nearest-neighbor shells. Variation of the parameter  $r_2$  can, therefore, be considered as giving a variable coupling between the impurity electron and the nearest-neighbor F shells.

The fact that the data are fitted with values of

$r_2$  large enough to reverse the effective charge of the F ions implies that little physical significance can be attached to these values of  $r_2$ . This conclusion is also supported by the results of another recent application<sup>11</sup> of the coupling model presented here. The application of uniaxial strain to the Eu<sup>2+</sup> ion in the fluorite lattices<sup>12</sup> results in the splitting of the lowest degenerate level of the  $4f^6 5d$  configuration by the  $E_g$  symmetry strain component and a shift of this level relative to the ground state by the  $A_{1g}$  strain component. The magnitudes of the splitting and shift per unit strain are proportional, respectively, to the magnitudes of the quadrupolar and monopolar coupling coefficients in Eq. (15). However, substantially larger values of  $r_2$  are required to fit these strain measurements than the values of  $r_2$  which best fit the impurity-induced Raman scattering. We may conclude from these results that the assumption of classical charge overlap does not give a very consistent description of the electron-phonon coupling problem. This implies that the inclusion of quantum-mechanical overlap and exchange effects is required. The latter can perhaps be accomplished by using a Slater exchange potential  $V_{ex} \sim \rho^{1/3}$ , where  $\rho$  is the electronic charge density. This potential has a similar effect on the electron-phonon coupling to that of increasing the classical charge overlap.

The failure of the extended-charge model to give a good fit to the Raman data in one portion of the acoustic region may also result from the truncation of expansion (7) or from the neglect of terms higher than quadrupolar in the potential-energy expansion. To include other terms adjustable parameters would be required to replace the first summation in Eq. (10). This is because the matrix elements  $\langle \alpha | r^p \Phi_n^{\Gamma}(\theta, \varphi) | \beta \rangle$  for all even  $p \leq n$  and all electronic states  $\alpha$  and  $\beta$  are unknown. However, it is likely that matrix-element selection rules for the energy levels of the impurity will limit the number of spherical harmonic terms required. For instance, the highest-order terms which would lead to a coupling within the  $5d$  and  $4f$  mainfolds are  $n=4$  and  $n=6$ , respectively. Since the  $4f$  electrons have much weaker coupling to the lattice than the  $5d$  electrons, only  $n=4$  terms are likely to be important.

### C. Weak Scattering in CaF<sub>2</sub>

The impurity-induced scattering from the Eu<sup>2+</sup> ions was observed to decrease in intensity progressively for the host series BaF<sub>2</sub>, SrF<sub>2</sub>, and CaF<sub>2</sub>. The reason for this behavior is not immediately obvious, since it is apparent from Table I that the Eu<sup>2+</sup> ion differs far more in size and electronic configuration from Ca<sup>2+</sup> than Sr<sup>2+</sup> or Ba<sup>2+</sup>. Furthermore, there is no evidence that the properties of the  $4f^6 5d$  configuration change greatly from one

host to another, since the absorption bands  $4f^7 \rightarrow 4f^6 5d$  are at about the same energy and show similar crystal-field splittings in all three hosts.<sup>13</sup> We have made the further observation that the intensities of the impurity-induced spectra scale among these crystals in rough proportion to the intensities of the one- and two-phonon scattering in the pure crystals. This evidence suggests that the  $f-d$  transitions may not be of primary importance in determining the change in the local polarizability derivatives as has been assumed in this work.<sup>14</sup>

### V. CONCLUSIONS

The primary results of this work has been the demonstration of the inadequacy of the nearest-neighbor coupling model for calculations of impurity-induced phonon spectra even in highly ionic crystals, such as the alkaline-earth fluorides. The apparent

success of this model is some of the alkali-halide lattices<sup>1</sup> is possibly due to the more similar anion and cation masses in the host crystals studied in Ref. 1. However, there remains the possibility that the electronic states responsible for the impurity scattering are perturbed band states in the fluorite systems discussed in this paper, whereas they are more localized for  $Tl^+$  in the alkali halides. This is unlikely, since the  $6s 6p$  excited states of the  $Tl^+$  ion, which are most likely the intermediate electronic states responsible for the scattering in the alkali halides,<sup>2</sup> are also not very well localized compared with inter-ion distances. We, therefore, feel that the nearest-neighbor coupling model will not give an accurate representation of the impurity-induced scattering in any but the simplest lattices in which all ions vibrate with roughly equal amplitudes throughout the phonon spectrum.

<sup>1</sup>Research supported by the National Science Foundation.

\*Alfred P. Sloan Foundation Fellow.

<sup>1</sup>Present address: Bayer AG, Leverkusen, West Germany.

<sup>1</sup>R. T. Harley, J. B. Page, Jr., and C. T. Walker, Phys. Rev. B **3**, 1365 (1971). This reference contains a brief review of the work in this area up to 1970.

<sup>2</sup>G. Benedek and N. Terzi, in *Proceedings of the Second International Conference on Light Scattering in Solids* (Flammarion, Paris, 1971), p. 291.

<sup>3</sup>D. H. Kuhner, H. V. Lauer, and W. E. Bron, Phys. Rev. B **5**, 4112 (1972).

<sup>4</sup>L. Couture and J. P. Mathieu, Ann. Phys. (N.Y.) **3**, 521 (1948).

<sup>5</sup>R. Loudon, Proc. Roy. Soc. A **275**, 218 (1963); Adv. Phys. **13**, 423 (1964).

<sup>6</sup>E. Loh, Phys. Rev. **175**, 533 (1968).

<sup>7</sup>C. J. Ballhausen, *Introduction to Ligand Field Theory* (McGraw-Hill, New York, 1962).

<sup>8</sup>R. Srivastava, H. V. Lauer, L. L. Chase, and W. E. Bron, Phys. Lett. A **36**, 333 (1971).

<sup>9</sup>W. H. Kleiner, J. Chem. Phys. **20**, 1784 (1952).

<sup>10</sup>R. G. Shulman and S. Sugano, Phys. Rev. Lett. **7**, 157 (1961).

<sup>11</sup>W. E. Bron, D. Kuhner, and A. Man, Bull. Am. Phys. Soc. **17**, 313 (1972).

<sup>12</sup>A. A. Kaplyanski and A. K. Przewusky, Opt. Spektrosk. **19**, 597 (1965) [Opt. Spectrosc. **19**, 331 (1965)].

<sup>13</sup>A. A. Kaplyanski and P. P. Feofilov, Opt. Spektrosk. **13**, 235 (1965) [Opt. Spectry. (USSR) **13**, 129 (1962)].

<sup>14</sup>Note added in proof: Recent Raman scattering measurements in  $BaF_2$  containing  $Ca^{2+}$  impurities and  $CaF_2$  containing  $Ba^{2+}$  impurities show no observable impurity-induced scattering. This suggests that neither perturbed electronic band states nor perturbed phonon eigenvectors contribute measurably to the scattering observed with  $Eu^{2+}$  impurities in the work reported here. The decreasing scattering efficiency of  $Eu^{2+}$  in the series  $BaF_2$ ,  $SrF_2$ ,  $CaF_2$  apparently results from the decrease in the electron-phonon coupling for the  $5d$  electron in these hosts. This effect is also apparent in the increase in the absorption strength of the zero-phonon lines of  $Eu^{2+}$  in this series (see Ref. 13).

## Thermal Conductivity of Cerium Magnesium Nitrate

J. P. Harrison and J. P. Pendry

*Department of Physics, Queen's University, Kingston, Ontario, Canada*

(Received 21 September 1972)

The thermal conductivity of cerium magnesium nitrate has been measured over the temperature range 0.2–1.5 °K. When an assumption is made that the surface of the crystal is damaged to a depth of 150  $\mu\text{m}$  by sandblasting, the conductivity measurements are entirely described by the Casimir theory of boundary scattering of phonons.

### I. INTRODUCTION

Cerium magnesium nitrate (CMN) is a Kramers salt that has been extensively investigated largely because of its application in low-temperature re-

frigeration and thermometry. Some years ago it was found that at very low temperatures the thermal relaxation between CMN and  $He^3$  was several orders of magnitude faster than expected either theoretically or empirically if judged by other